PHYSICAL REVIEW MATERIALS **6**, 043603 (2022)

Deformation-induced medium-range order changes in bulk metallic glasses

Keita Nomoto,[1,2] Bosong Li,[1] Christoph Gammer,[3] Anna V. Ceguerra,[2] Huma Bilal,[2] Anton Hohenwarter,[4]
Jürgen Eckert,[3,4] Bernd Gludovatz,[1] Simon P. Ringer,[2] and Jamie J. Kruzic[1,*]
[1]*School of Mechanical and Manufacturing Engineering, University of New South Wales (UNSW Sydney), Sydney, Australia*
[2]*The University of Sydney, Australian Centre for Microscopy & Microanalysis, and School of Aerospace, Mechanical and Mechatronic Engineering, Sydney, Australia*
[3]*Erich Schmid Institute of Materials Science, Austrian Academy of Sciences, Leoben, Austria*
[4]*Department of Materials Science, Chair of Materials Physics, Montanuniversität Leoben, Leoben, Austria*

(Received 3 February 2022; revised 16 March 2022; accepted 4 April 2022; published 25 April 2022)

Bulk metallic glasses (BMGs) naturally have excellent strength and elasticity while structural rejuvenation into higher energy glassy states is often required to improve ductility. However, our understanding of the detailed atomic ordering changes that occur during rejuvenation processes, such as plastic deformation, remains limited. This study utilizes nanobeam electron diffraction in a transmission electron microscope as an effective method to reveal the structural changes that occur after deformation in two Zr-based BMGs. Our findings indicate that heavy deformation from indentation or fracture causes an increase in the size of fcc-like medium-range order (MRO) clusters in a harder icosahedral dominated matrix, which corresponds to local softening of the BMGs. By examining the structure evolution at different points in the fracture process, we reveal that the mechanism of growth of MRO clusters is likely driven by enhanced diffusion from local temperature rise and/or free volume generation rather than deformation-induced nucleation and growth of new MRO sites.

DOI: 10.1103/PhysRevMaterials.6.043603

I. INTRODUCTION

Bulk metallic glasses (BMGs) represent a class of metallic alloys that are well known for a lack of long-range structural order along with excellent strength and elasticity properties [1–3]. However, achieving good ductility in BMGs remains a challenge and extensive research has been undertaken to understand how to control the glassy structures of BMGs to achieve improved deformability. Structural relaxation of BMGs to denser and lower energy states (e.g., by annealing below the glass transition temperature T_g) has long been known to embrittle BMGs [4–11]; thus, research efforts have focused on how to induce structural rejuvenation to higher energy glassy structures to improve ductility and fracture toughness [12]. Various methods to induce structural rejuvenation have been reported, such as elastostatic compression [13–15], cryogenic thermal cycling (TC) [16–20], high-pressure torsion (HPT) deformation [21–24], cold rolling [25–31], and mechanical imprinting [32–34]. Other examples of activating higher energy glassy structures are achieved by forming nanoglasses by electrodeposition [35] or pulling a BMG rod sample to apply strain during cooling [36]. While such studies have revealed clear connections between increased relaxation enthalpy and softening of BMGs, macroscopic ductility and toughness are also thought to be related to heterogeneities in the glassy structure at multiple length scales [18,21,22,27–29,32,34,37]. Furthermore, our understanding of how detailed structural features at the atomistic scale, such as short-range order (SRO) and medium-range order (MRO), as well as features at the microscale control the deformation response remains limited [38–40].

Recently, nanobeam electron diffraction (NBED) and fluctuation electron microscopy (FEM) studies in a transmission electron microscope (TEM) have revealed a linear relationship between the local hardness of the BMG and the MRO cluster size and volume fraction at the nanoscale [38]. While the scaling of the relationship was found to be sensitive to BMG composition, the linear relationship was identical for different rejuvenation treatments that altered the local hardness such as cryogenic thermal cycling, high-pressure torsion deformation, or cold rolling, i.e., a location with identical hardness in both treated and untreated samples had identical MRO cluster size and volume fraction regardless of the sample history [38]. With this finding, we proposed a model that explains how the volume fraction and size of the relatively soft fcc-like clusters in a harder matrix dictate the local hardness of BMGs. Thus, the analysis of MRO using the NBED-based technique appears to be a viable method to further understand deformation-induced structural changes that occur in BMGs during much more severe deformation processes such as indentation or catastrophic fracture.

Accordingly, in this study the same two zirconium-based BMGs as in Ref. [38] were used to study the local MRO changes induced by indentation and bulk fracture processes. We first confirm the repeatability of our previous correlation between local hardness and MRO using uniaxial compression samples that can be easily cross sectioned and hardness

---

[*] Corresponding author: j.kruzic@unsw.edu.au

mapped. We then use NBED and FEM to examine TEM samples taken from the plastic zones of indents and from fracture surfaces to measure the local MRO and estimate the amount of deformation-induced softening. Our findings indicate that those heavy deformation processes cause an increase in the size of fcc-like MRO clusters in a harder icosahedral dominated matrix, which corresponds to local softening of the BMG. This study helps to establish NBED-based MRO analysis as a viable method for examining deformation-induced structural changes in BMGs and creating a better understanding of BMG deformation mechanisms.

II. MATERIALS AND METHODS

A. Materials

The $Zr_{63.78}Cu_{14.72}Ni_{10}Al_{10}Nb_{1.5}$ BMG used in this study was prepared by suction copper mold casting in Ar (99.999%) atmosphere as described in detail previously [18]. The thermally cycled (TC) samples used in this study were treated by alternatingly immersing the samples into liquid nitrogen and boiling water for 1 min each for a total of 170 cryogenic thermal cycles. Research grade $Zr_{52.5}Cu_{17.9}Ni_{14.6}Al_{10}Ti_5$ (at. %) BMG plates were procured from Liquidmetal Technologies (USA). Annealing of the Zr-Cu-Ni-Al-Ti BMG was conducted at 630 K for 2 h under an Ar atmosphere using a heat flux calorimeter (DSC 204 F1, Netzsch).

B. Mechanical testing

Uniaxial compression testing was conducted for the as-cast Zr-Cu-Ni-Al-Nb BMG samples using ($N = 5$) rectangular specimens with nominal dimensions of $2\times2\times4\,\mathrm{mm}^3$ that were cut from larger beam samples using a low-speed diamond saw. The surfaces were ground flat and parallel prior to testing using a computer-controlled servo-hydraulic testing machine (Model 8872, Instron Corporation, Norwood, MA, USA) with a calibrated 25-kN load cell. The displacement rate used for the compression tests was 0.33 μm/s and the true plastic strain (ε_t) was calculated to account for the cross-sectional area change by $\varepsilon_t = \ln(1 + L/L_0)$, where L_0 and L are the initial and final sample length, respectively. After the compression test, samples were cut perpendicular to the length and the cross section was polished for subsequent microhardness mapping. Microhardness mapping with more than 1400 indents (Durascan-80, Struers, Denmark) was conducted on the polished cross sections with an applied load of 0.05-kg force and a dwell time of 10 s. An indent spacing of 40 μm was selected to balance mapping spatial resolution with the ability to map large areas while avoiding interference between the indents that would occur if the spacing was too small, as described in more detail in our previous studies [18,29,38].

To examine the effect of heavy deformation on the BMG structure, two types of samples were used: (1) indent plastic zones and (2) fracture surfaces. For the former case, larger dimension microhardness indents were produced to create a large plastic zone full of visible shear bands. Those larger indents were prepared on polished surfaces for an as-cast (AC) Zr-Cu-Ni-Al-Ti BMG sample and a thermally cycled (TC) Zr-Cu-Ni-Al-Nb BMG sample using the same microhardness tester with an applied load of 1-kg and 0.5-kg force, respectively, and a dwell time of 10 s. These indentation loads were 10–20 times larger than the loads used in our microhardness mapping, and the plastic zone radii of the large indents were calculated to be ~35 and ~50 μm for the Zr-Cu-Ni-Al-Nb BMG and the Zr-Cu-Ni-Al-Ti BMG, respectively [41,42]. TEM specimens were then lifted out from the heavily shear-banded regions of the plastic zone, as shown in Fig. 2(e). Fracture surface samples for both AC and TC Zr-Cu-Ni-Al-Nb BMG samples were taken from a previous study [18]. In brief, $2\times4\times20\,\mathrm{mm}^3$ beam single edge notched bending samples were tested in three-point bending using a 15-mm loading span on a computer-controlled servo-hydraulic testing machine (Model 8872, Instron Corporation, Norwood, MA, USA) with a 5-kN load cell and a constant displacement rate of 0.83 μm/s. For the AC and annealed Zr-Cu-Ni-Al-Ti BMGs samples, plates were cut into $0.5\times1\times6\,\mathrm{mm}^3$ beam samples that were micronotched to approximately half the sample width. Three-point bending fracture toughness tests were conducted using a 4-mm loading span on a screw-driven 2-kN bending stage (Deben UK Ltd., London, UK) with a 150-N load cell and a constant displacement rate of 0.55 μm/s.

C. Structural and chemical characterization

The TEM specimens were produced by a standard lift-out method [43] using a xenon plasma focused ion beam scanning electron microscope (PFIB-SEM, Helios G4 PFIB, Thermo-Fisher Scientific, USA). The lifted-out sample with Pt/C protection layer was thinned at 30 kV and 30–300 pA for coarse milling and at 5 kV and 30 pA for fine milling. The incident angle of the ion beam to the TEM lamella was restricted within ±2° from the parallel angle to avoid a potential damage from the ion beam. TEM experiments were conducted using a JEM-2200FS (JEOL, Japan) at an acceleration voltage of 200 kV. For pair distribution function (PDF) determination, selected area electron diffraction (SAED) patterns were acquired at an exposure time of 2 s using an energy slit of 5 eV together with a selected area aperture (10 μm) and entrance aperture (120 μm). The camera length was set at 300 mm and calibrated in diffraction mode using {200} reflections from gold nanoparticles standard sample to avoid any artefacts caused by the microscope settings. The diffraction pattern collected using these settings was from a selected area of around 200 nm in diameter, meaning the signal contains both the ordered clusters and the less ordered matrix. The PDF was calculated using in-house developed software called EDP2PDF to extract an azimuthally integrated diffraction pattern from the SAED pattern and to convert it to the structure function and PDF, as described elsewhere [44–47]. The background in the integrated diffraction intensity was detected and removed using a sensitive nonlinear iterative peak clipping algorithm [48]. The range of the scattering vector to obtain the PDF was ~1.1–8.1 Å^{-1} extracted from the SAED profile. Nanobeam electron diffraction (NBED) experiments were carried out using a condenser aperture size of 40 μm and the nanometer-size electron beam diameter R ($R = 0.7$–1.6 nm) as full width at half maximum of the Gaussian intensity distribution. A fixed semiconvergence angle around 2.75 ± 0.11 mrad was calculated by the diameter of the transmitted beam ($2.19 \pm 0.09\,\mathrm{nm}^{-1}$). The probe current density for the beam sizes of

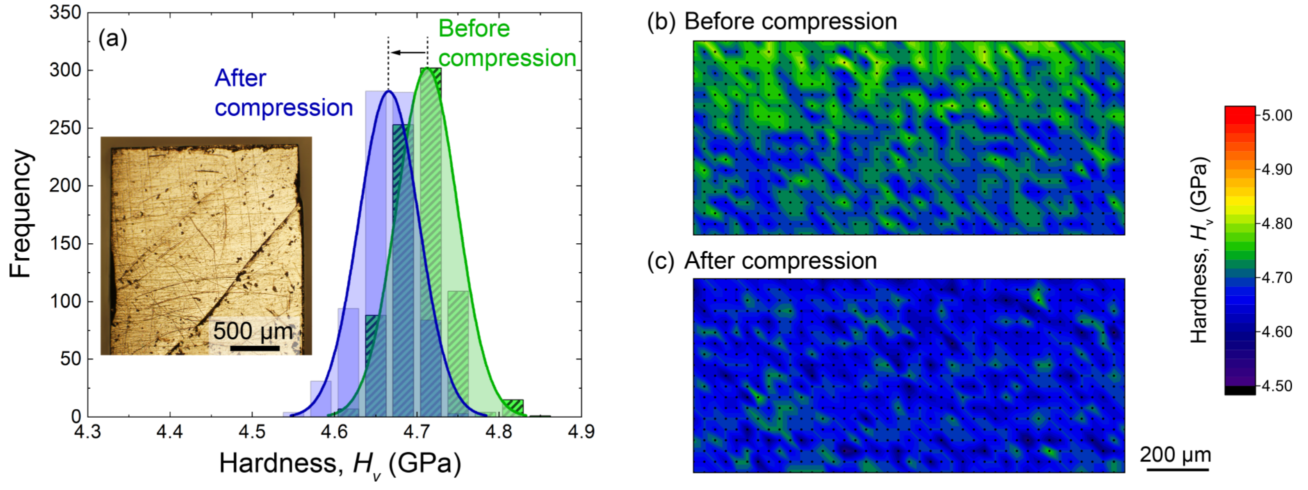

FIG. 1. (a) Hardness histogram before and after mechanically loading as-cast Zr-Cu-Ni-Al-Nb BMG in compression to ~1.5% true plastic strain. The histogram bin size was 0.033 GPa and the curves represent a normal distribution fit to the data. The inset is a photograph of the deformed sample. Microhardness maps taken (b) before and (c) after testing.

0.7, 1.0, 1.3, and 1.6 nm were 4.3, 5.7, 7.5, and 10.2 $\mathrm{pA/cm^2}$, respectively. A raster of 15×15 NBED patterns was recorded using an energy slit of 10 eV at different exposure time (3–0.5 s) at binning 4 (1024×1024 pixel size) for each sample, and fluctuation electron microscopy (FEM) [49] was used to extract the MRO cluster size, as described in Refs. [38,50–52]. The annular integrated variance and mean variance were calculated on a pixel by pixel basis [53] as a function of the k value using PASAD tools [54] and custom script in DigitalMicrograph™ [55]. The MRO cluster size W and characteristic length scale Λ ($\Lambda = W/\sqrt{10}$) were calculated from the slope and intercept of linear Q^2/V versus Q^2 plots using nanobeam diameters R ranging 0.7–1.6 nm. The function of $\sqrt{10}$ is to estimate the average size of clusters, assuming their shape is a spheroid as described in Ref. [49]. V (k,Q) is the normalized variance of the diffracted intensity from NBED experiments, and Q (=0.61/R) is the radius of the virtual objective aperture used during FEM [50–52]. The first two peak positions of V (k,Q) were read at approximately 3.6 and 4.5 $\mathrm{nm^{-1}}$ using a custom MATLAB script and the error analysis for the MRO cluster size is explained in the Supplemental Material [56]. The explanation of these parameter selections can be found in our previous study [38].

The atom probe tomography (APT) measurements were conducted using a LEAP4000XSi system (CAMECA, USA) equipped with a 355-nm laser and ~57% detector efficiency. The atom probe tips lifted out via SEM-FIB (Auriga, Zeiss, Germany) were cooled to ~40 K and the measurements were run in the $10^{-11} - 10^{-12}$ Torr range in the analysis chamber. The laser power, laser pulse repetition rate, and detection rate were 75 pJ, 160 kHz, and 3%, respectively. Three-dimensional (3D) reconstructions were carried out using the commercially available IVAS® software (version 3.8.4 and AP Suite 6.0). Reconstruction parameters used for the analysis were a field factor of 3.3, an image compression factor of 1.65, and a field evaporation of 29 V/nm.

III. RESULTS

A. Softening during compression deformation

Figure 1 shows microhardness results for an as-cast (AC) sample of the $\mathrm{Zr_{63.78}Cu_{14.72}Ni_{10}Al_{10}Nb_{1.5}}$ (at. %) BMG that was compressed to ~1.5% true plastic strain [inset in Fig. 1(a)] to introduce structural changes throughout the sample. Here, we refer to the global applied true strain that considers the changing cross section of the sample (see the Methods section) while recognizing that the strain inside and outside of shear bands is not constant. The maximum true plastic strain to failure for various compression samples we made from this BMG ranged from 4 to 10%, and we arrested the deformation at a compressive strain that ensured failure would not occur. Hardness distributions taken from cross sections before and after compression are compared in Fig. 1(a), revealing a shift in the hardness distribution to lower values. A similar decrease in the average hardness after compression testing was confirmed for four samples. Cross sections of the exact same sample are compared in Fig. 1 before and after compression testing since the initial hardness deviates slightly from one sample to another. Hardness maps are shown in Figs. 1(b) and 1(c) to allow visualization of the 2D hardness distribution on the sample cross sections. The average hardness of the compressed samples decreases approximately ~0.05 GPa, and considerable overlap remains in the hardness distributions measured before and after compression. Thus, for relatively mild deformation processes there are many locations within a sample with identical hardness, and thus identical MRO size and volume fraction determined by NBED [38], both before and after deformation.

B. Structural changes after deformation

A broad range of samples was examined in the TEM, including polished cross sections of known hardness as well as fracture surfaces and shear band regions in the plastic zones around indents. For the fracture surfaces, any locally

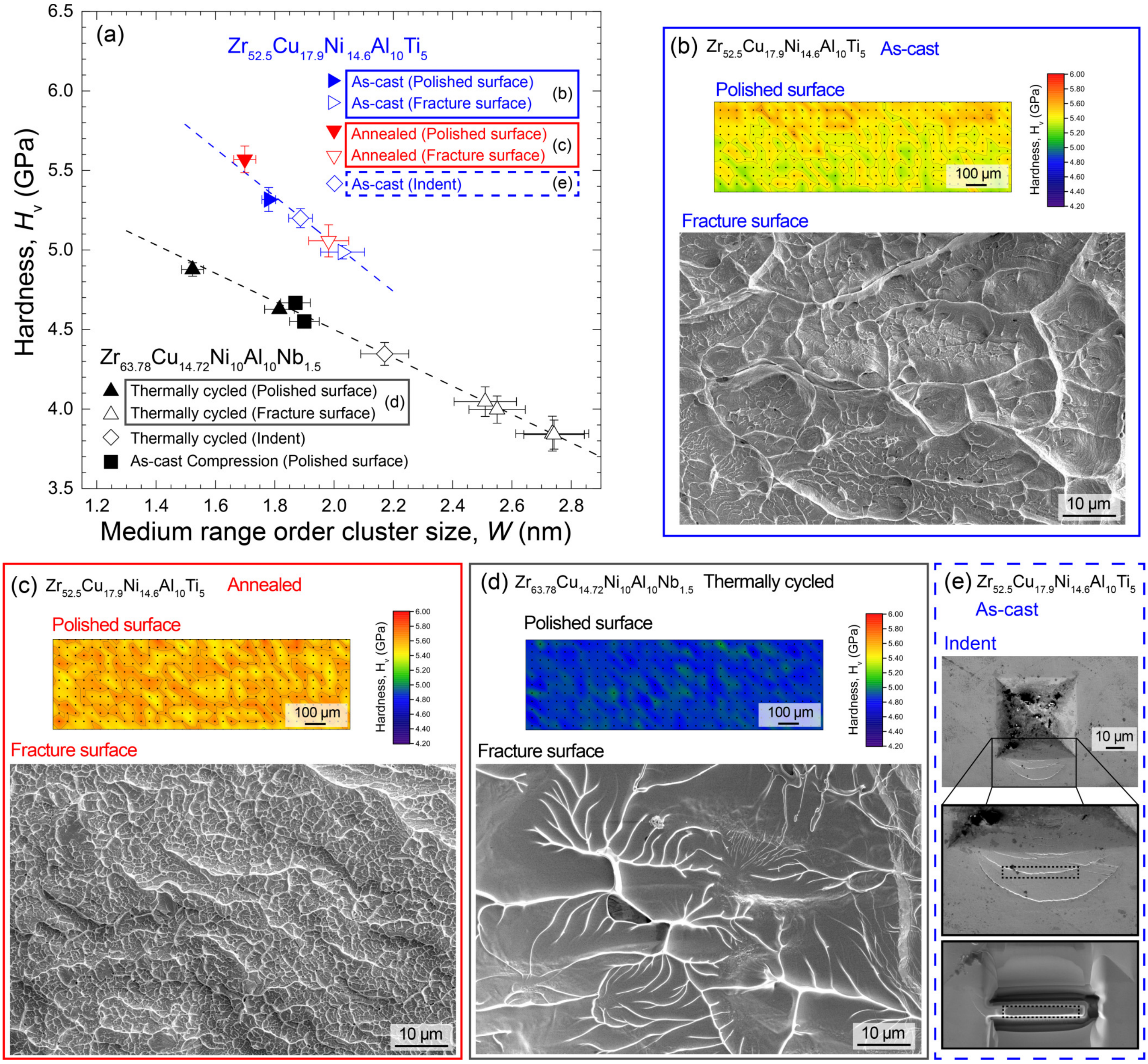

FIG. 2. (a) Hardness versus medium-range order (MRO) cluster size. Solid symbols represent new data from this study with known hardness, open symbols represent MRO measurements from indent plastic zones or fracture surfaces with unknown hardness, and the dashed lines are the trendlines determined in Ref. [38]. The error bars represent standard deviation for the hardness value and standard error for the MRO cluster size. The hardness values of indent plastic zones or fracture surfaces were estimated based on the measured MRO values and the extrapolated linear relationships determined in Ref. [38]. (b)–(d) Microhardness maps and micrographs of fracture surfaces for the Zr-Cu-Ni-Al-Ti and Zr-Cu-Ni-Al-Nb BMGs and (e) micrograph of the plastic zones around an indent for the Zr-Cu-Ni-Al-Ti BMG. The TEM lamella was taken from the area of the dashed rectangular region within the indent plastic zone.

melted regions on fracture surfaces were avoided and regions ~200 nm deep below the heavily deformed fracture surface were examined in this study. Table S1 of the Supplemental Material [56] gives a list of the samples used in this study and, when known, their average hardness. Figure 2(a) compares the MRO cluster sizes for the various deformed and undeformed samples summarized in Supplemental Material Table S1. The dashed lines in Fig. 2(a) represent the linear relationships between the MRO cluster size and the local hardness of the $Zr_{63.78}Cu_{14.72}Ni_{10}Al_{10}Nb_{1.5}$ and $Zr_{52.5}Cu_{17.9}Ni_{14.6}Al_{10}Ti_5$ (at. %) BMGs found in our previous study [38]. For the uniformly compressed samples, where hardness mapping was conducted on the sample cross sections, we selected TEM samples from locations between four indents whose hardness variation was minimal (the standard deviation of hardness values from four indents is ~0.02 GPa) to make sure that the MRO cluster size accurately reflects the local hardness. Indeed, Fig. 2(a) shows an excellent agreement between the compression samples measured in this study and the relationship between local hardness and MRO determined in Ref. [38]. It is important to note that the sampling volume of the MRO measurements was many orders of magnitude smaller than that of the hardness measurements. Thus, a key aspect for connecting the nanoscale nature of the MRO measurements and the micro/mesoscale nature of the hardness mapping was having regions of uniform hardness over tens or hundreds of micrometers where both hardness and MRO sampling could be performed in the same location, as was confirmed in Ref. [38]. We do not anticipate this relationship would be easy to determine in the presence of steep hardness gradients where it would be difficult to accurately assess the hardness at the location of MRO sampling.

TEM was used to evaluate the nearest neighbor distances from PDF that were calculated from SAED patterns. Figure S1 of the Supplemental Material [56] shows that the PDF analysis reveals no clear correlation of average nearest neighbor distances with known hardness values, and no discernable trend for the heavily deformed fracture surfaces and indent plastic zones. While it is possible that localized SRO changes are outside the resolution of our TEM based PDF measurements, there was no easily measured structural signature of deformation in the PDFs that we measured. Using atom probe experiments we also confirmed that neither nanocrystals nor chemical segregation occurred on the fracture surfaces of the HPT deformed samples as shown in Fig. S2 (see the Supplemental Material [56]). Thus, NBED-based MRO analysis provides an effective method to discern structural changes that are otherwise unobservable using TEM-based PDF analysis.

Samples taken from fractured beam specimens or from indent plastic zones [Figs. 2(b)–2(e), open symbols in Fig. 2(a)] had unknown local Vickers microhardness values because the hardness on uneven surfaces (e.g., on the shear bands or fracture surfaces) is not reliably measurable and accurate microhardness measurement requires a flat, well prepared surface. In those cases, the estimated hardness values are plotted in Fig. 2(a) based on the measured MRO values and the extrapolated linear relationships determined in Ref. [38] (dashed lines). Since all new data in this study with known hardness matches the previous relationship [i.e., comparing the closed symbols in Fig. 2(a) to the dashed lines], we have high confidence in the robustness of the linear relationships. For cryogenically thermally cycled $Zr_{63.78}Cu_{14.72}Ni_{10}Al_{10}Nb_{1.5}$ samples, the MRO cluster sizes ($\sim$1.5–1.8 nm) for the polished sides of the samples (closed triangles) fall in the same range as found in Ref. [38]. In contrast, the range of MRO cluster sizes for the deformed region around an indent (open diamond) or for a fracture surface (open triangle) greatly exceeds ($\sim$2.2–2.8 nm) the range observed for polished samples with the same thermal history [closed triangles in Fig. 2(a) and data in Ref. [38]]. Such results suggest that a large amount of structural change, consistent with softening, occurs due to these heavy deformation processes, i.e., much more than could be achieved by uniaxial compression (solid squares). Comparing the solid and open symbols for the $Zr_{52.5}Cu_{17.9}Ni_{14.6}Al_{10}Ti_5$ BMG reveals a similar trend for both BMGs, where the fracture surfaces and indent plastic zones exhibit much larger MRO cluster sizes than the polished side of the as-cast and annealed samples [Fig. 2(a)].

The feature sizes on the fracture surfaces of the annealed and embrittled $Zr_{52.5}Cu_{17.9}Ni_{14.6}Al_{10}Ti_5$ BMG samples [Fig. 2(c)] are much smaller than for the as-cast samples [Fig. 2(b)], as is expected from the literature [57]. After the fracture process was completed, the annealed samples still show a smaller MRO cluster size compared to as-cast samples, suggesting that some of the initial difference in hardness was retained even after the heavy deformation processes that occur during fracture [Fig. 2(a)]. To further understand the evolution of structural changes in MRO during the fracture process, TEM lamellae were taken from three distinct regions, *R*(I)–*R*(III), that commonly define the fracture process of ductile BMGs [34,58,59]. In Fig. 3(a), crack propagation was initiated in a thermally cycled $Zr_{63.78}Cu_{14.72}Ni_{10}Al_{10}Nb_{1.5}$ sample from the end of a fatigue precrack (left side) and proceeded to the right side, as indicated by the arrow. *R*(I) is seen as a relatively smooth region of the fracture surface immediately adjacent to the fatigue precrack with multiple intersecting shear bands and is produced by a quasistatic crack tip blunting process. *R*(II) is the so-called Tylor meniscus instability zone that represents the first crack initiation process caused by the separation of a dominant shear band, while *R*(III) is associated with the dynamic fast fracture process. Figure 3 shows the different features on the fracture surface of the thermally cycled Zr-Cu-Ni-Al-Nb BMG and compares their associated MRO cluster sizes. The results reveal that the MRO cluster size fluctuates between 2.5 and 2.8 nm [Fig. 3(b)], including for different locations within *R*(I), and there is no clear trend for the different fracture surface regions. Thus, the quasistatic versus dynamic nature of the different fracture surfaces has a negligible effect on the observed changes in MRO.

IV. DISCUSSION

The mechanistic correlation between lower hardness and a larger size and higher volume fraction of MRO clusters was previously explained by a nanocomposite model of softer fcc-like MRO sites acting as shear transformation zone (STZ) nuclei within a harder matrix where icosahedral structure dominates [38]. In the present study, structural changes in deformed regions of two BMGs indicate an increase in MRO cluster size, which is associated with material softening. Furthermore, the present results highlight the need to carefully consider the amount of deformation and the location of sample collection when interpreting MRO changes. For heavy deformation (i.e., fracture surfaces or indent plastic zone), the MRO size shifts significantly to 2.5–2.8 nm and is unmistakably larger compared to the MRO size at any location in the undeformed sample. In contrast, for a more moderate amount of deformation (i.e., for samples compressed uniformly to $\sim$1.5% true plastic strain), the hardness range overlaps considerably before and after deformation [Fig. 1(a)]. Thus, choosing TEM samples from random locations in the heterogeneous microstructure may lead to erroneous conclusions (e.g., no MRO change), or could be inconclusive (e.g., random MRO change). In this case, observing the trend of MRO increase with deformation would require either sampling regions of known hardness, or conducting a broad statistical sampling and averaging from many samples.

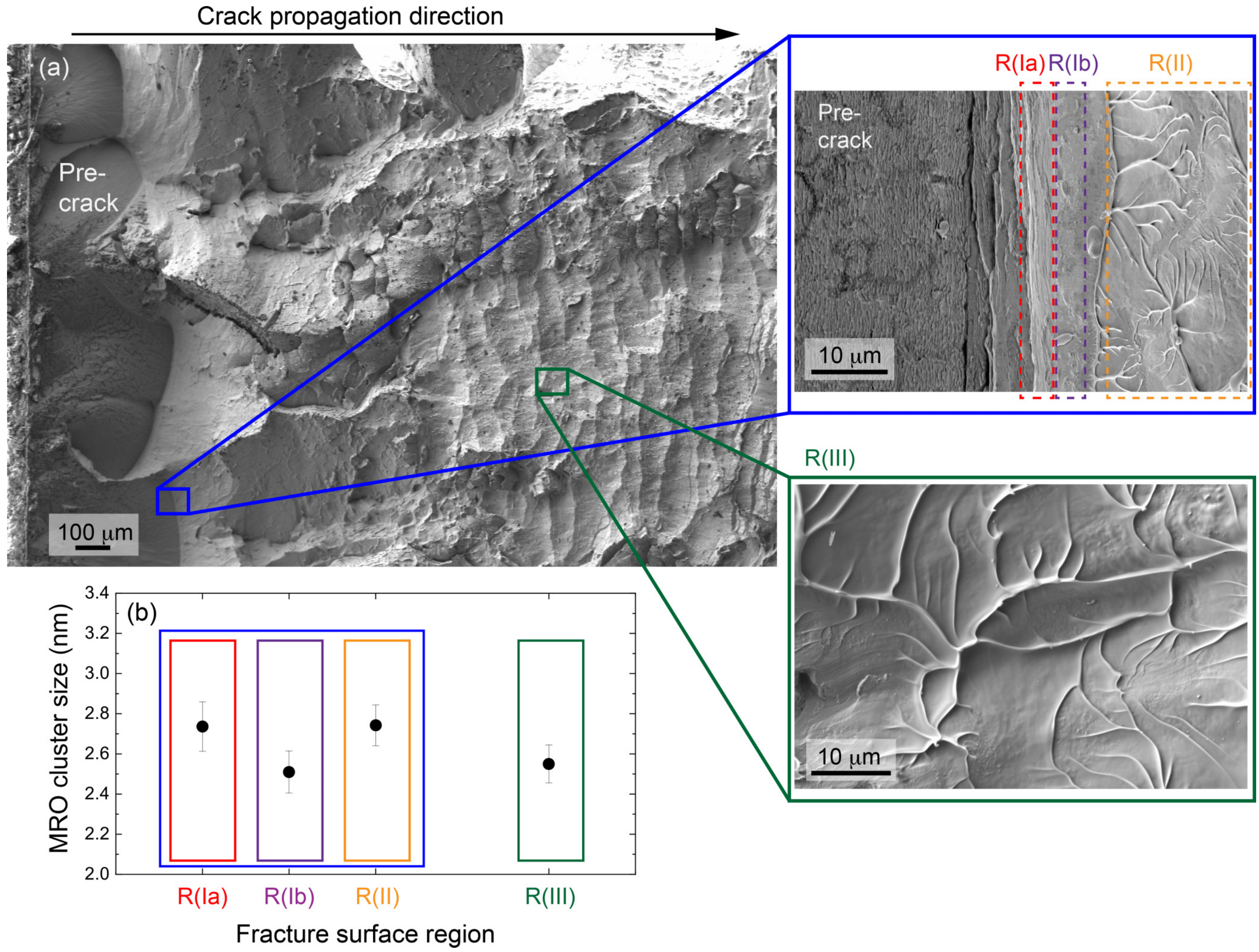

FIG. 3. (a) Fracture surface of a thermally cycled Zr-Cu-Ni-Al-Nb BMG. (b) MRO cluster size at different types of the fracture surface. The arrow in (a) indicates the direction of crack propagation from the left side to the right side. The error bars represent standard error for the MRO cluster size.

While it must be recognized that the quantitative accuracy of the linear relationship between the hardness and the MRO cluster size is less certain when extrapolated to the larger MRO size ranges observed after heavy deformation, the concept of structural rejuvenation due to plastic deformation is well established and thus the qualitative correlation here is clear, i.e., heavy deformation causes an increase in MRO cluster size which can be correlated with local softening.

The mechanism for the MRO size increase during deformation remains unclear thus far. Hilke *et al.* [39] have also demonstrated that the MRO cluster size in a shear band region is larger than that in the adjacent matrix and suggested that either frictional heat dissipation combined with enhanced diffusion [60–62] or shear-induced nucleation and growth [63] may account for the increases in the MRO cluster size. For the latter case, Mura *et al.* described a mechanism of shear-induced transport of atoms to crystal nuclei in liquids and deduced that the shear flow rate significantly affects the nucleation rate [63]. When considering the results of the present study, despite the varying fracture surface morphology of the sample shown in Fig. 3 and the variation from slow quasistatic deformation of *R*(I) to fast deformation in *R*(III), a trend in MRO cluster size is not evident. Thus, during the fracture process, quasistatic crack tip deformation appears equally effective in inducing MRO structural changes as dynamic fracturing, and this lack of rate dependence suggests that shear-enhanced nucleation of MRO sites is not the likely mechanism. Additionally, Ding *et al.* [64] have demonstrated that large amounts of rejuvenation and structural rearrangement can occur by shock compression of BMG samples over time scales of <400 ns, further suggesting that nucleation processes are not involved in the mechanism.

For the case of heat dissipation and enhanced diffusion, it was argued that shear localization and shear banding cause a local temperature rise [60,61,65,66]. While there is no general agreement regarding the magnitude of the temperature rises that are induced during deformation, nearing or exceeding the glass transition temperature during fracture is well accepted [65,67,68]. Furthermore, irrespective of any possible temperature rise, tracer diffusion experiments after deformation is completed have shown increased diffusivity up to eight orders of magnitude for deformed samples containing shear bands due to the local increases in free volume creating short-circuit diffusion paths [62,69]. Recently, Shen *et al.* [70] revealed the formation of discrete nanocavities as a mechanism governing the fracture process of various glasses, and it was suggested that the nanocavities are nucleated by enhanced atomic diffusion. Thus, enhanced diffusion may arise from both a temperature rise and free volume generation and overall it is likely that there is capacity for atomic rearrangements to facilitate the growth of MRO clusters during deformation. Furthermore, this effect need not be limited to the interior of the shear bands but may extend into the shear band affected zone. Indeed, nanoindentation studies have shown a softened zone extending tens to hundreds of micrometers from shear bands [71]; a recent x-ray photon correlation spectroscopy study suggested structurally effected zones extending tens of micrometers [72], while a recent TEM study has reported MRO changes extending several micrometers from shear bands [73]. Furthermore, enhanced transport may also be expected in regions containing embryonic shear bands where only partial percolation of STZs is achieved but a fully developed shear band is unable to form. Finally, it is possible that residual stresses between the shear bands may relax after deformation and mechanically induce structural changes. Uncovering the exact mechanisms for structural changes outside of the shear bands, and understanding how far those structural changes extend, will require significant, further research.

While this study focuses on the rationales behind the growth of fcc-like MRO clusters with deformation, it is worth noting that another report shows that a deformation process caused an overall reduction of MRO symmetry. While at first glance these results might seem in contradiction, they can be rationalized as follows. *In situ* NBED experiments have suggested that plastic deformation degrades the degree of twofold and fourfold symmetry in a Zr-Cu-Al BMG [74]; however, such experiments are only able to measure a net effect of the changes in all nanoscale structures containing those symmetries. In other words, in a glassy nanocomposite where softer fcc-like MRO clusters sit in a harder icosahedral dominated matrix [38], it would be impossible to deconvolute how deformation separately affects the different nanostructures simply by tracking the twofold and fourfold symmetry. Furthermore, molecular dynamics (MD) modeling of the same Zr-Cu-Al BMG showed that the decrease in twofold and fourfold symmetry was likely associated with a disordering of icosahedral structures [74]. More recent experiments used 4D-scanning transmission electron microscopy (STEM) with a PDF analysis of a $Zr_{52.5}Cu_{17.9}Ni_{14.6}Al_{10}Ti_5$ BMG to reveal that geometrically favored icosahedral short-range order motifs decrease in shear bands and shear band affected zones [75]. Similarly, other MD studies of binary Zr-Cu BMGs have reported deformation to induce a disordering of fully icosahedral SRO sites [76,77]. Feng *et al.* further found that relatively softer SRO clusters (as compared with fully icosahedral clusters) tend to connect with each other to form larger MRO aggregates and networks [77]. Thus, it is reasonable to assume that the disordering of icosahedral sites in the harder matrix could account for the loss of twofold and fourfold symmetry observed in Ref. [74] even if the fcc-like MRO clusters simultaneously grow in size.

Finally, the structural changes caused by both moderate and heavy deformation did not result in measurable shifts in the TEM-based PDF nearest neighbor peak positions, which suggests that MRO measurement is a more robust way to measure deformation-induced structural changes. While the recent 4D-STEM results of Mu *et al.* suggest that changes indeed occur at the first and second nearest neighbors, those measurements were highly localized at shear bands and in shear band affected zones [75]. Similarly, Liu *et al.* observed the first TEM diffraction pattern ring to shift in peak position inside the shear band relative to the matrix [78]. Since the present study did not specifically compare the interior regions of shear bands to the matrix, it is not surprising that such changes in SRO were not observed.

V. CONCLUSIONS

This study focuses on the nanostructural changes of the medium-range order (MRO) in BMGs after various deformation processes. Our findings suggest that the size of relatively soft fcc-like MRO clusters increases in deformed samples in proportion to the severity of deformation, with samples taken from the plastic zones of indents and fracture surfaces of broken samples exhibiting much larger increases in the MRO cluster size than were seen in our previous work. The collective information suggests that a complicated deformation process involves phenomena including local heat generation, enhanced diffusion, growth of fcc-like MRO clusters, and disordering of icosahedral motifs. In this scenario, we suggest that shear localization generates local heat and free volume increases, and enhanced diffusion promotes growth of fcc-like MRO clusters. This is also thought to occur simultaneously with the destruction of geometrically favored icosahedral motifs in the harder, surrounding matrix. TEM-based MRO analysis using nanobeam electron diffraction and fluctuation electron microscopy appears to be an excellent tool to measure and monitor BMG structure changes that are induced to improve the ductility and fracture toughness and build mechanistic models for structure property relationships in BMGs.

ACKNOWLEDGMENTS

The authors acknowledge the use of the facilities and the scientific and technical assistance of Sydney Microscopy & Microanalysis (SMM), a core research facility of the University of Sydney and a node of Microscopy Australia. We thank Dr. H. Liu from SMM for his support in the PDF analysis. This research was supported by the Australian Research Council Discovery Grant No. DP180101393. B.G. additionally acknowledges support from the Australian Research Council Future Fellowship (Project No. FT190100484) and the UNSW Scientia Fellowship schemes. Finally, support was provided through the European Research Council under the Advanced Grant “INTELHYB – Next Generation of Complex Metallic Materials in Intelligent Hybrid Structures” (Grant No. ERC-2013-ADG-340025).

[1] T. C. Hufnagel, C. A. Schuh, and M. L. Falk, Acta Mater. **109**, 375 (2016).
[2] A. C. Lund and C. A. Schuh, Philos. Mag. Lett. **87**, 603 (2007).
[3] C. Suryanarayana and A. Inoue, *Bulk Metallic Glasses* (CRC Press, Boca Raton, Florida, 2017).
[4] M. E. Launey, R. Busch, and J. J. Kruzic, Scr. Mater. **54**, 483 (2006).
[5] M. E. Launey, R. Busch, and J. J. Kruzic, Acta Mater. **56**, 500 (2008).
[6] J. J. Kruzic, Adv. Eng. Mater. **18**, 1308 (2016).
[7] R. L. Narayan, P. Tandaiya, R. Narasimhan, and U. Ramamurty, Acta Mater. **80**, 407 (2014).
[8] R. Gerling, F. P. Schimansky, and R. Wagner, Acta Metall. **36**, 575 (1988).
[9] P. Murali and U. Ramamurty, Acta Mater. **53**, 1467 (2005).
[10] J. J. Lewandowski, W. H. Wang, and A. L. Greer, Philos. Mag. Lett. **85**, 77 (2005).
[11] T. W. Wu and F. Spaepen, Philos. Mag. B **61**, 739 (1990).
[12] Y. Sun, A. Concustell, and A. L. Greer, Nat. Rev. Mater. **1**, 16039 (2016).
[13] K. W. Park, C. M. Lee, M. Wakeda, Y. Shibutani, E. Fleury, and J. C. Lee, Scr. Mater. **59**, 710 (2008).
[14] K. W. Park, C. M. Lee, M. Wakeda, Y. Shibutani, M. L. Falk, and J. C. Lee, Acta Mater. **56**, 5440 (2008).
[15] M. Zhang, Y. M. Wang, F. X. Li, S. Q. Jiang, M. Z. Li, and L. Liu, Sci. Rep. **7**, 625 (2017).
[16] S. V. Ketov, Y. H. Sun, S. Nachum, Z. Lu, A. Checchi, A. R. Beraldin, H. Y. Bai, W. H. Wang, D. V. Louzguine-Luzgin, M. A. Carpenter, and A. L. Greer, Nature **524**, 200 (2015).
[17] S. Y. Di, Q. Q. Wang, J. Zhou, Y. Y. Shen, J. Q. Li, M. Y. Zhu, K. B. Yin, Q. S. Zeng, L. T. Sun, and B. L. Shen, Scr. Mater. **187**, 13 (2020).
[18] B. S. Li, S. H. Xie, and J. J. Kruzic, Acta Mater. **176**, 278 (2019).
[19] J. Ketkaew, R. Yamada, H. Wang, D. Kuldinow, B. S. Schroers, W. Drnowski, T. Egami, and J. Schroers, Acta Mater. **184**, 100 (2020).
[20] A. Das, E. M. Dufresne, and R. Maass, Acta Mater. **196**, 723 (2020).
[21] Y. B. Wang, D. D. Qu, X. H. Wang, Y. Cao, X. Z. Liao, M. Kawasaki, S. P. Ringer, Z. W. Shan, T. G. Langdon, and J. Shen, Acta Mater. **60**, 253 (2012).
[22] X. L. Bian, D. Zhao, J. T. Kim, D. Sopu, G. Wang, R. Pippan, and J. Eckert, Mater. Sci. Eng. A **752**, 36 (2019).
[23] S. H. Joo, D. H. Pi, A. D. H. Setyawan, H. Kato, M. Janecek, Y. C. Kim, S. Lee, and H. S. Kim, Sci. Rep. **5**, 9660 (2015).
[24] C. Ebner, B. Escher, C. Gammer, J. Eckert, S. Pauly, and C. Rentenberger, Acta Mater. **160**, 147 (2018).
[25] M. H. Lee, K. S. Lee, J. Das, J. Thomas, U. Kühn, and J. Eckert, Scr. Mater. **62**, 678 (2010).
[26] Y. Yokoyama, K. Yamano, K. Fukaura, H. Sunada, and A. Inoue, Scr. Mater. **44**, 1529 (2001).
[27] Q. P. Cao, J. W. Liu, K. J. Yang, F. Xu, Z. Q. Yao, A. Minkow, H. J. Fecht, J. Ivanisenko, L. Y. Chen, X. D. Wang, S. X. Qu, and J. Z. Jiang, Acta Mater. **58**, 1276 (2010).
[28] S. Scudino, B. Jerliu, K. B. Surreddi, U. Kühn, and J. Eckert, J. Alloys Compd. **509**, S128 (2011).
[29] B. S. Li, S. Scudino, B. Gludovatz, and J. J. Kruzic, Mater. Sci. Eng. A **786**, 139396 (2020).
[30] S. H. Xie and J. J. Kruzic, J. Alloys Compd. **694**, 1109 (2017).
[31] M. Stolpe, J. J. Kruzic, and R. Busch, Acta Mater. **64**, 231 (2014).
[32] S. Scudino, B. Jerliu, S. Pauly, K. B. Surreddi, U. Kühn, and J. Eckert, Scr. Mater. **65**, 815 (2011).
[33] S. Scudino, J. J. Bian, H. S. Shahabi, D. Sopu, J. Sort, J. Eckert, and G. Liu, Sci. Rep. **8**, 9174 (2018).
[34] B. S. Li, H. S. Shahabi, S. Scudino, J. Eckert, and J. J. Kruzic, Mater. Sci. Eng. A **646**, 242 (2015).
[35] Q. Yang, C.-Q. Pei, H.-B. Yu, and T. Feng, Nano Lett. **21**, 6051 (2021).
[36] R. M. O. Mota, E. T. Lund, S. Sohn, D. J. Browne, D. C. Hofmann, S. Curtarolo, A. van de Walle, and J. Schroers, Commun. Mater. **2**, 23 (2021).
[37] Y. H. Liu, G. Wang, R. J. Wang, D. Q. Zhao, M. X. Pan, and W. H. Wang, Science **315**, 1385 (2007).
[38] K. Nomoto, A. V. Ceguerra, C. Gammer, B. Li, H. Bilal, A. Hohenwarter, B. Gludovatz, J. Eckert, S. P. Ringer, and J. J. Kruzic, Mater. Today **44**, 48 (2021).
[39] S. Hilke, H. Rösner, D. Geissler, A. Gebert, M. Peterlechner, and G. Wilde, Acta Mater. **171**, 275 (2019).
[40] F. A. Davani, S. Hilke, H. Rösner, D. Geissler, A. Gebert, and G. Wilde, J. Appl. Phys. **128**, 015103 (2020).
[41] K. L. Johnson, *Contact Mechanics* (Cambridge University Press, Cambridge, UK, 1985).
[42] J. J. Kruzic, D. K. Kim, K. J. Koester, and R. O. Ritchie, J. Mech. Behav. Biomed. **2**, 384 (2009).
[43] P. Felfer, T. Li, K. Eder, H. Galinski, A. P. Magyar, D. C. Bell, G. D. W. Smith, N. Kruse, S. P. Ringer, and J. M. Cairney, Ultramicroscopy **159**, 413 (2015).
[44] B. E. Warren, J. Appl. Phys. **8**, 645 (1937).
[45] C. L. Farrow and S. J. L. Billinge, Acta Cryst. A **65**, 232 (2009).
[46] Y. Q. Cheng, E. Ma, and H. W. Sheng, Phys. Rev. Lett. **102**, 245501 (2009).
[47] Y. J. Sun, D. D. Qu, Y. J. Huang, K. D. Liss, X. S. Wei, D. W. Xing, and J. Shen, Acta Mater. **57**, 1290 (2009).
[48] M. Morháč, J. Kliman, V. Matoušek, M. Veselský, and I. Turzo, Nucl. Instrum. Methods Phys. Res. A **401**, 113 (1997).
[49] J. M. Gibson, M. M. J. Treacy, and P. M. Voyles, Ultramicroscopy **83**, 169 (2000).
[50] J. Hwang and P. M. Voyles, Microsc. Microanal. **17**, 67 (2011).
[51] S. N. Bogle, L. N. Nittala, R. D. Twesten, P. M. Voyles, and J. R. Abelson, Ultramicroscopy **110**, 1273 (2010).
[52] M. M. J. Treacy, J. M. Gibson, L. Fan, D. J. Paterson, and I. McNulty, Rep. Prog. Phys. **68**, 2899 (2005).
[53] T. L. Daulton, K. S. Bondi, and K. F. Kelton, Ultramicroscopy **110**, 1279 (2010).
[54] C. Gammer, C. Mangler, C. Rentenberger, and H. P. Karnthaler, Scr. Mater. **63**, 312 (2010).
[55] C. Gammer, B. Escher, C. Ebner, A. M. Minor, H. P. Karnthaler, J. Eckert, S. Pauly, and C. Rentenberger, Sci. Rep. **7**, 44903 (2017).
[56] See Supplemental Material at http://link.aps.org/supplemental/10.1103/PhysRevMaterials.6.043603 for sample list in this study, short-range order analysis, atom probe data, and error bar analysis.
[57] X. K. Xi, D. Q. Zhao, M. X. Pan, W. H. Wang, Y. Wu, and J. J. Lewandowski, Phys. Rev. Lett. **94**, 125510 (2005).

[58] P. Tandaiya, R. Narasimhan, and U. Ramamurty, Acta Mater. **61**, 1558 (2013).
[59] R. Narasimhan, P. Tandaiya, I. Singh, R. L. Narayan, and U. Ramamurty, Int. J. Fracture **191**, 53 (2015).
[60] A. J. Cao, Y. Q. Cheng, and E. Ma, Acta Mater. **57**, 5146 (2009).
[61] J. J. Lewandowski and A. L. Greer, Nat. Mater. **5**, 15 (2006).
[62] J. Bokeloh, S. V. Divinski, G. Reglitz, and G. Wilde, Phys. Rev. Lett. **107**, 235503 (2011).
[63] F. Mura and A. Zaccone, Phys. Rev. E **93**, 042803 (2016).
[64] G. Ding, C. Li, A. Zaccone, W. H. Wang, H. C. Lei, F. Jiang, Z. Ling, and M. Q. Jiang, Sci. Adv. **5**, eaaw6249 (2019).
[65] A. Das, P. Kagebein, S. Küchemann, and R. Maaß, Appl. Phys. Lett. **112**, 261905 (2018).
[66] P. Thurnheer, F. Haag, and J. F. Loffler, Acta Mater. **115**, 468 (2016).
[67] C. J. Gilbert, J. W. A. III, V. Schroeder, R. O. Ritchie, J. P. Lloyd, and J. R. Graham, Appl. Phys. Lett. **74**, 3809 (1999).
[68] C. J. Gilbert, V. Schroeder, and R. O. Ritchie, Metall. Mater. Trans. A **30**, 1739 (1999).
[69] I. Binkowski, G. P. Shrivastav, J. Horbach, S. V. Divinski, and G. Wilde, Acta Mater. **109**, 330 (2016).
[70] L.-Q. Shen, J.-H. Yu, X.-C. Tang, B.-A. Sun, Y.-H. Liu, H.-Y. Bai, and W.-H. Wang, Sci. Adv. **7**, eabf7293 (2021).
[71] R. Maass, P. Birckigt, C. Borchers, K. Samwer, and C. A. Volkert, Acta Mater. **98**, 94 (2015).
[72] S. Küchemann, C. Liu, E. M. Dufresne, J. Shin, and R. Maaß, Phys. Rev. B **97**, 014204 (2018).
[73] F. A. Davani, S. Hilke, H. Rosner, D. Geissler, A. Gebert, and G. Wilde, J. Alloys Compd. **837**, 155494 (2020).
[74] T. C. Pekin, J. Ding, C. Gammer, B. Ozdol, C. Ophus, M. Asta, R. O. Ritchie, and A. M. Minor, Nat. Commun. **10**, 2445 (2019).
[75] X. Mu, M. R. Chellali, E. Boltynjuk, D. Gunderov, R. Z. Valiev, H. Hahn, C. Kübel, Y. Ivanisenko, and L. Velasco, Adv. Mater. **33**, 2007267 (2021).
[76] D. Şopu, A. Stukowski, M. Stoica, and S. Scudino, Phys. Rev. Lett. **119**, 195503 (2017).
[77] S. Feng, L. Qi, L. Wang, S. Pan, M. Ma, X. Zhang, G. Li, and R. Liu, Acta Mater. **95**, 236 (2015).
[78] C. Liu, Z. Cai, X. Xia, V. Roddatis, R. Yuan, J. M. Zuo, and R. Maaß, Scr. Mater. **169**, 23 (2019).